Aberrations of varied line-space grazing incidence gratings in converging light beams

Michael C. Hettrick

Applied Optics Vol. 23, Issue 18, pp. 3221-3235 (1984)

http://dx.doi.org/10.1364/AO.23.003221

Aberrations of varied line-space grazing incidence gratings in converging light beams

Michael C. Hettrick

Analytic calculations are presented which describe aberrations of the in-plane and off-plane varied line-space grating designs we recently proposed [Appl. Opt. 22, 3921 (1983)]. Ray traces confirming these results to within typical accuracies of 10% are illustrated for several examples. Spectral field aberrations are calculated for convenient focal surfaces, and optimal field curvatures are calculated and ray traced. An improvement of the off-plane fan grating is proposed, where the angular spacings of the grooves are varied to achieve a large decrease in grating aberrations. However it is shown that, in conical diffraction, the net resolution can also be dominated by a diminished dispersive power compared to in-plane grating mounts. Curved groove in-plane grating designs are ray traced, revealing no substantial degradation in imaging performance by restricting such curves to concentric circles. However, it is also shown that the general case of hyperbolic grooves can be fabricated by use of visible or UV holography, with small residual aberrations. We designate this new class of holographic gratings as Type V. Misalignment aberrations of high resolution in-plane gratings, for the *in situ* cases of off-axis illumination, grating and detector displacements, and grating rotational misalignment, are calculated and found to be generally small.

I. Introduction

In a recent communication,[1] we presented two general designs of grazing incidence gratings which constitute a new geometric class of spectrometers. This class consists of a plane reflection grating which intercepts light which otherwise would converge to a single imaging focus. This focus is thereby reflected to a stigmatic point corresponding to the zero-order (or $\lambda = 0$) image off the grating. Aberration correction of nonzero wavelengths is then provided through a smooth spatial variation in the grating constant. In the simplest cases, this variation is over only one of the pupil coordinates, leading to either in-plane straight parallel grooves or off-plane straight fan grooves. In the more advanced designs, the remaining higher-order aberrations (dominantly coma) are removed by curvature of the grooves. Recently, we uncovered several interesting papers by Murty[2,3] and Hall[4] in which some aspects of this approach were previously investigated at normal incidence. A thesis by Baumgardner[5] on the aberration correction of concave gratings also proposed unusual groove patterns having some similarities with our work. Cash[6] also recently discussed a design related to one of the two subclasses which we have proposed.

In this paper we explicitly derive the imaging results reported in our previous communication. In Sec. II, the grating aberrations are expanded as power series in the grating pupil coordinates and are compared to ray traces. Ray traces are also used to confirm the growth in aberrations away from the aberration-corrected wavelength for various focal surfaces. Section III presents an analysis of dispersive aberrations resulting from the finite size of the zero-order image and the finite dispersive power of the gratings as situated in converging light. Comparisons are made between the resulting performance limits for in-plane vs off-plane grating mounts. In Sec. IV we extend our analysis of this class of gratings to include calculations of aberrations resulting from both translational and rotational misalignments of the collecting mirror, grating, and detector. Section V summarizes this work.

II. Grating Aberrations

In this section we assume the grating is fed by a collecting mirror which brings light to a perfect focus at a fixed point in space. Our analysis of the resulting grating aberrations uses the light-path function to determine wave front aberrations and employs Fermat's principle to convert these into focal plane aberrations of the images. Aberrations will be expressed as polynomials in the grating pupil coordinates by use of power series expansions.

The author is with University of California, Space Sciences Laboratory, Berkeley, California 94720.

Received 20 April 1984.
0003-6935/84/183221-15$02.00/0.

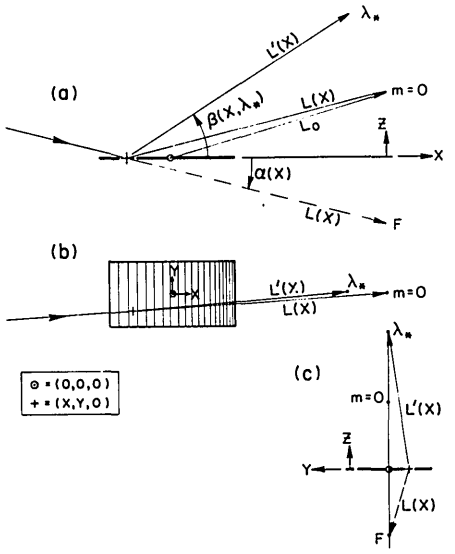

Fig. 1. In-plane orthogonal coordinate system. Projections are displayed on the (a) central dispersion plane $y = 0$, (b) grating plane $z = 0$, and (c) a plane $x = t_0$. The 3-D distances are indicated rather than the projected distances.

A. Straight and Parallel In-Plane Grooves

Figure 1 shows the projection of our straight groove in-plane grating geometry on an orthogonal coordinate system. The x axis is perpendicular to the rulings and passes through the grating midplane. The z axis is perpendicular to the grating plane, therefore the dispersed spectrum lies in the x-z plane, which is also a plane of symmetry for the converging light beam. The y axis is collinear with the central ruling of the grating and lies in the grating plane. The origin of this orthogonal coordinate system is located at the geometric center of the grating.

1. *Imaging at a Correction Wavelength*

With straight and parallel grooves, varied line spacing provides perfect focusing along the x axis for a preselected wavelength $\lambda*$. The functional variation of the line-spacing $d(x)$ is given in Ref. 1 and can also be expressed implicitly in terms of the x coordinate for the Nth groove:

$$mN\lambda* = \sqrt{(t_1 - x_N)^2 + h_1^2} - \sqrt{(t_0 - x_N)^2 + h_0^2} - P_0, \quad (1)$$

as shown in Fig. 2, where (t_1,h_1) and (t_0,h_0) are Cartesian distance parameters to the focal positions of $\lambda*$ and $\lambda = 0$, respectively, and where P_0 is the path-length difference for groove $N = 0$, constrained to be at $x = 0$:

$$P_0 = \sqrt{t_1^2 + h_1^2} - \sqrt{t_0^2 + h_0^2}. \quad (2)$$

We remark that Eq. (1) assigns negative values of m to inside spectral orders. This is the European convention, however the opposite convention is of equal popularity.

To calculate the aberrations resulting from violation of Eq. (1) for $y \neq 0$, let $L(x,y,0)$ denote the distance from any point $(x,y,0)$ on the grating pupil to the mirror

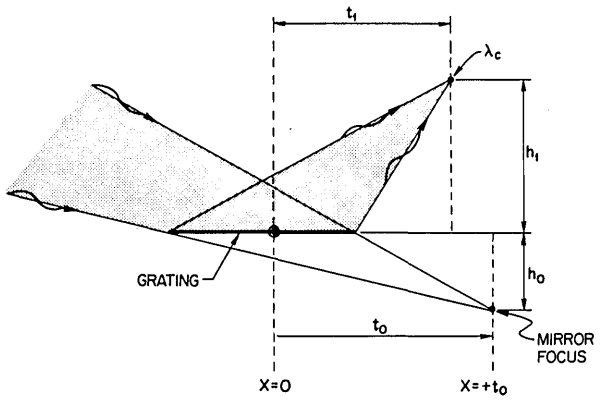

Fig. 2. Distance parameters which specify the in-plane grating geometry.

focus. Due to the plane grating surface, this distance also equals that to the zero-order image. Also let $L'*(x,y,0)$ denote the distance to the focal position of $\lambda*$. The path-length difference $L' - L$ defines the shift in wave fronts which interfere at the focal surface. For a perfect (stigmatic) focus at $\lambda*$, this difference must jump by the quantity $m\lambda*$ between adjacent grooves, where m is the spectral order. If the groove $x = 0$ is assigned $N = 0$, the error in the wave front (the error in the light-path function) is

$$\Delta* = L'* - L + mN\lambda* - [L'*(0,0,0) - L(0,0,0)]. \quad (3)$$

The bracketed term is P_0 as defined above. For straight grooves, anastigmatic focusing along the central groove ($x = 0$) requires $L'*(0,0,0) = L(0,0,0) \equiv L_0$, so P_0 vanishes. However, even if nonzero, it would not contribute to any derivatives of Δ. From Fig. 1(a), we derive

$$L = \sqrt{L_0^2 \sin^2\alpha_0 + (L_0 \cos\alpha_0 - x)^2 + y^2};$$

$$L'* = \sqrt{L_0^2 \sin^2\beta_0 + (L_0 \cos\beta_0 - x)^2 + y^2};$$

and, since the line spacing is adjusted to yield $\Delta* = 0$ along $y = 0$, we find

$$mN\lambda* = \sqrt{L_0^2 \sin^2\alpha_0 + (L_0 \cos\alpha_0 - x)^2} - \sqrt{L_0^2 \sin^2\beta_0 + (L_0 \cos\beta_0 - x)^2}.$$

Expressing all distances in units of L_0:

$$L = \sqrt{1 - 2x \cos\alpha_0 + x^2 + y^2};$$

$$L'* = \sqrt{1 - 2x \cos\beta_0 + x^2 + y^2}, \quad (4a)$$

$$mN\lambda* = \sqrt{1 - 2x \cos\alpha_0 + x^2} - \sqrt{1 - 2x \cos\beta_0 + x^2}. \quad (4b)$$

Expanding the radicals and taking advantage of the fact that only terms containing y^2 and differing between L and $L'*$ will contribute to $\Delta*$, we have the result reported previously[1]:

$$\Delta* = (\cos\beta_0 - \cos\alpha_0)[1/2xy^2 + 3/4x^2y^2(\cos\beta_0 + \cos\alpha_0) - 3/8xy^4 + \ldots]$$
$$= (m\lambda*/d)[1/2xy^2 + 3/4x^2y^2(\cos\beta_0 + \cos\alpha_0) - 3/8xy^4 + \ldots]. \quad (5)$$

By use of Fermat's condition, the wave front aberration Δ can be converted into image aberrations $\Delta\lambda$ and H, where $\Delta\lambda$ is the extremum ray wavelength extent of the image in the dispersion direction, and H is the extremum ray image height perpendicular to the dispersion direction. The general relations connecting wave front and image aberrations for an in-plane grating are[7]

$$\lambda/\Delta\lambda = (m\lambda/d_0)/(\delta\Delta/\delta x), \tag{6a}$$

$$H = \delta\Delta/\delta y, \tag{6b}$$

where all distances are in units of L_0. Since this distance is used to obtain the above relations and will vary in small amounts across the resulting finite size image, these equations are accurate only to the fifth order in the grating coordinates, which is sufficient for the present analysis. Differentiating $\Delta*$, we have

$$\delta\Delta*/\delta x = (m\lambda*/d_0)[1/2\, y^2 + 3/2\, xy^2(\cos\beta_0 + \cos\alpha_0) + \ldots], \tag{7a}$$

$$\delta\Delta*/\delta y = (m\lambda*/d_0)(xy + 3/2\, x^2y - 3/2\, xy^3 + \ldots). \tag{7b}$$

Since $y = \pm L_0/(2f_y)$ and $x = \pm L_0(\alpha_{\max} - \alpha_{\min})/(2\alpha_{\max})$ at the edges of the grating, the extremum image aberrations for a filled rectangular aperture are

$$\lambda*/\Delta\lambda* = 8f_y^{-2} + \ldots, \tag{8a}$$

$$H*/L_0 = (m\lambda*/d_0)/(2\alpha_{\max}f_xf_y), \tag{8b}$$

where $f_x \equiv 1/(\alpha_{\max} - \alpha_{\min})$. Note that $\lambda/\Delta\lambda$ is independent of the graze angle, allowing the same imaging properties in the limit as the graze angle vanishes.

Figure 3(c) confirms the above predictions, where the system parameters are those of the short-wavelength flight spectrometer for the Extreme Ultraviolet Explorer (EUVE) satellite:

$L_0 = 485.2$ mm;	$t_0 = 481.5$ mm;	$h_0 = 59.9$ mm;
$P_0 = 0.26$ mm;	$t_1 = 463.9$ mm;	$h_1 = 143.1$ mm;
$f_y = 6.24$;	$d_0 = 4350$ Å;	$\lambda* = 160$ Å; $m = -1$.

The graze angle of incidence therefore ranges from $\alpha = 6.02° - 8.62°$, resulting in $f_x \simeq 22$ over a ruled width of 173.16 mm. The resolving power is $\lambda*/\Delta\lambda* \simeq 300$ and the image height $H* \simeq 0.4$ mm. The plate scale is ~2.64 Å/mm at $\lambda*$, which combined with a collecting mirror focal length of 1361.4 mm yields ~0.5 Å/min of arc of sky. The image shapes reveal the presence of coma, which is predicted by Eq. (5) to limit the resolution.

2. *Spectral Field Aberrations*

The flat grating surface provides stigmatism at $\lambda = 0$, and the variation in line spacing is chosen to provide stigmatism or quasi-stigmatism at a selected $\lambda*$. In general, this class of designs therefore has very wide wavelength coverage at moderate resolution, given a suitably chosen focal surface. Specifically, in this section we consider the growth in aberrations as one moves away from $\lambda*$ for the straight groove grating.

Ray traced in Fig. 3 are the aberrations over a broad range in wavelength. The wavelength at which maximum wavelength correction was enforced, $\lambda*$, is 150 Å for this example. The degradation in image quality as one moves away from $\lambda*$ depends on the shape of the focal surface. We consider two cases: a planar detector and a spherical detector. (As the spectrum falls within the x-z plane, a spherical detector is virtually equivalent to a cylindrical detector.) A straightforward calculation yields the analytic result for grating aberrations along a spherical detector centered at the grating geometric center (0,0,0) with radius equal to L_0. First, we generalize Eq. (3) for wavelengths λ not necessarily equal to $\lambda*$:

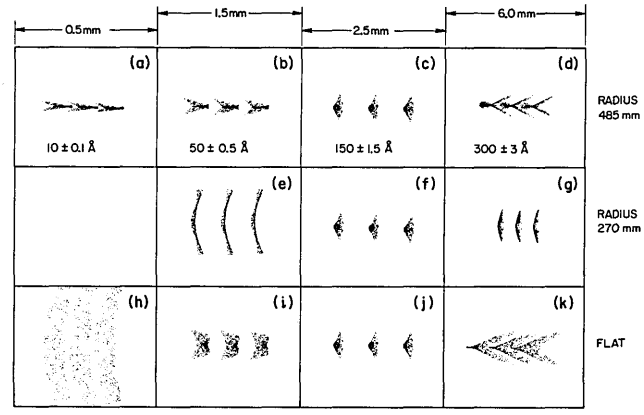

Fig. 3. Ray trace spot diagrams for the straight groove in-plane grating specified in the text but with $\lambda* = 150$ Å: (a)–(d) along the sagittal circle of radius L_0; (e)–(g) along the tangential circle of radius $0.56\, L_0$; and (h)–(k) along a plane passing through $\lambda*$. Wavelengths within each of the triplets are separated by $\Delta\lambda/\lambda = 0.01$. Linear scales are indicated at the top.

$$\begin{aligned}\Delta &= \Delta* + (L' - L + mN\lambda) - (L'* - L + mN\lambda*)\\ &= L' - L'* + mN(\lambda - \lambda*),\end{aligned} \tag{9}$$

where

$$\begin{aligned}L' &= \sqrt{1 - 2x\cos\beta + x^2 + y^2};\\ L'* &= \sqrt{1 - 2x\cos\beta_0 + x^2 + y^2};\end{aligned} \tag{10a}$$

$$\begin{aligned}mN(\lambda - \lambda*) = (\lambda/\lambda* - 1)(&\sqrt{1 - 2x\cos\alpha_0 + x^2}\\ &- \sqrt{1 - 2x\cos\beta_0 + x^2}).\end{aligned} \tag{10b}$$

From the grating equation we derive the difference relations,

$$\cos\beta_0 - \cos\alpha_0 = (m\lambda*/d_0), \tag{11a}$$

$$\cos\beta - \cos\alpha_0 = m\lambda/d_0, \tag{11b}$$

$$\cos\beta_0 - \cos\beta = (m/d_0)(\lambda* - \lambda), \tag{11c}$$

which when substituted into the series expansion of Eq. (9) yield

$$\begin{aligned}\Delta - \Delta* = (m/d_0)[&-1/2\, xy^2(\lambda* - \lambda)\\ &+ 1/2\,(m\lambda/d_0)(\lambda* - \lambda)x^2 + \ldots]\cdot\end{aligned} \tag{12}$$

Using the result previously obtained for $\Delta*$ [Eq. (5)], note that $\Delta = 0$ at $\lambda = 0$, as required by the plane grating surface. Taking the derivatives $\delta/\delta x$ and $\delta/\delta y$:

$$\delta\Delta/\delta x = 1/2\,(m\lambda/d_0)[y^2 + 2xm(\lambda* - \lambda)/d_0], \tag{13a}$$

$$\delta\Delta/\delta y = (m\lambda/d_0)xy. \quad (13b)$$

By use of Eqs. (6a) and (6b), these wave front errors yield focal aberrations:

$$\lambda/\Delta\lambda = 8/[f_y^{-2} + 8|m(\lambda* - \lambda)/d_0|/(f_x\alpha_0)], \quad (14a)$$

$$H/L_0 = (m\lambda/d_0)/(2\alpha_{max}f_xf_y). \quad (14b)$$

Therefore, the spectral aberration $\Delta\lambda$ has an additional term which increases linearly with the departure from $\lambda*$ and is proportional to the grating ruled width. The astigmatism has the same dependence as at $\lambda*$ and is linear with wavelength. The ray trace results of Figs. 3(a)–(d) and Fig. 4 confirm the above formulas along the sagittal cylinder. Thus, although $\Delta\lambda$ is minimized at $\lambda*$, the (sagittal) surface which minimizes H away from this point gives rise to various $\Delta\lambda$ which may be unnecessarily large.

The field curvature for minimization of $\Delta\lambda$ in the immediate vicinity of $\lambda*$ has been numerically calculated in the limit as the ruled width vanishes. The upper dotted curve in Fig. 5 shows the results plotted vs β/α. The optimal detector radius typically lies within the 0.5–0.65 L_0 range. Over finite ranges in wavelength and using finite grating sizes, this radius systematically decreases into the 0.4–0.5 L_0 range as shown by the lower dotted curve. The ray trace results for this tangential cylinder, shown in Figs. 3(e)–(g) and Fig. 4(a), reveal a significant improvement in spectral range and result from a detector curvature which minimizes $\Delta\lambda$ at $\lambda*/2$, $\lambda*$, and $3/2\lambda*$. A plane detector can be made to pass through $\lambda*$ and also through a second focal point. For the ray traces of Figs. 3(h)–(k), this second point was chosen as that which minimizes the astigmatism at 80 Å. The resulting detector pitch angle also passes near the point of minimum $\Delta\lambda$ for $\lambda \simeq 20$ Å, as revealed by the second relative maximum in Fig. 4(a). The spectral resolution in this figure is derived from 1-D binning of the extremum rays, and thus underestimates both the FWHM resolution and the resolution achievable with a 2-D imaging detector, as evident in Fig. 3.

B. Curved Groove In-Plane Designs

In the limit of an illuminating curve of infinitesimal width, $y = f(x)$, straight grooves can always provide a point image at $\lambda*$ by appropriate choice of groove spacing. However, to obtain such stigmatic focusing given illumination over a finite area on the grating pupil, the grooves must be curved. While the large spatial variation of the groove spacings in the x direction brings all light to the same focus at $\lambda*$ for $y = 0$, only a slight curvature of the grooves is required to maintain the same focus for all other cross sections $y \neq 0$.

1. *Holographic Ruling*

The interference fringes from coherent light sources located at the two stigmatic points ($m = 0$ and $\lambda*$) will record the corresponding stigmatic groove pattern.[1,2] Figure 6(b) shows a ray trace for an EUV curved groove grating, using the tangential focal surface derived above. This requires the central groove to be straight, resulting in hyperbolas on either side which curve in opposite

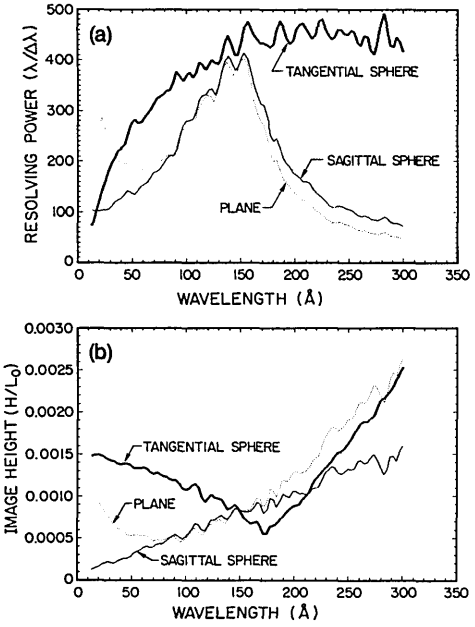

Fig. 4. Curves of extremum aberrations in wavelength and image height as functions of wavelength for the straight groove grating of Fig. 3. Results obtained through 1-D binning of numerical ray tracing. Bumps in the data signify only smoothed statistical noise.

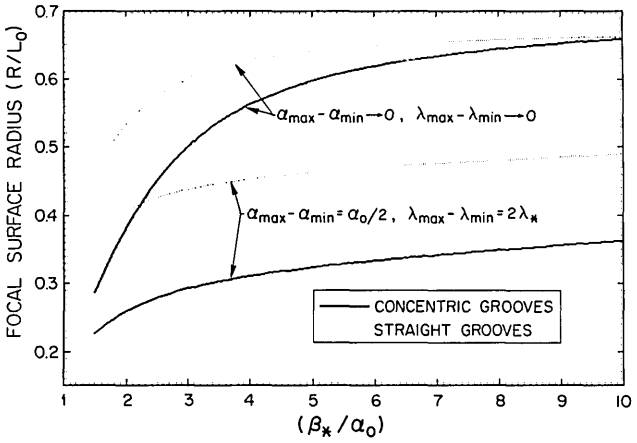

Fig. 5. Field curvature for minimization of wavelength aberrations for in-plane grating geometries.

directions [compare Fig. 1(c) of Ref. 1]. The correction wavelength is at 304 Å, near which an enormous increase in spectral resolution is revealed in comparison to the straight groove ray trace of Fig. 6(a). Even far away from this stigmatic wavelength, the spectral resolution is significantly higher, and the focal surface images are straight for this curved groove design.

However, the recording wavelength in the above example must equal $m\lambda*$. Given use at extreme UV wavelengths $\lambda* \sim 100$–1000 Å, the grating must operate in spectral orders $m \sim 10$ if conventional visible lasers ($\lambda_R \geq 3637$ Å) are used as the light sources. In the soft x-ray band, $\lambda* \sim 10$–100 Å, spectral orders $m \sim 100$ must be used, suggesting an echelle grating. However, to operate efficiently in spectral orders higher than the

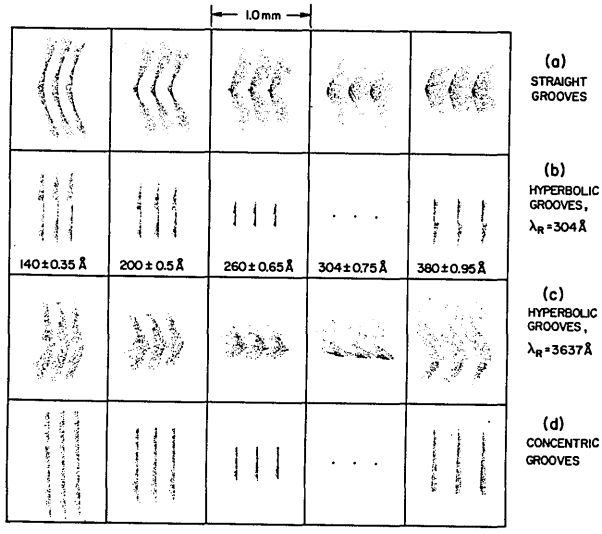

Fig. 6. Ray trace spot diagrams for (a) straight grooves, (b) stigmatic hyperbolas, (c) quasi-stigmatic hyperbolas generated by visible holography, and (d) concentric grooves. In all cases, the tangential focal surfaces have been employed, and each wavelength in the triplets is separated by $\Delta\lambda/\lambda = 1/400$.

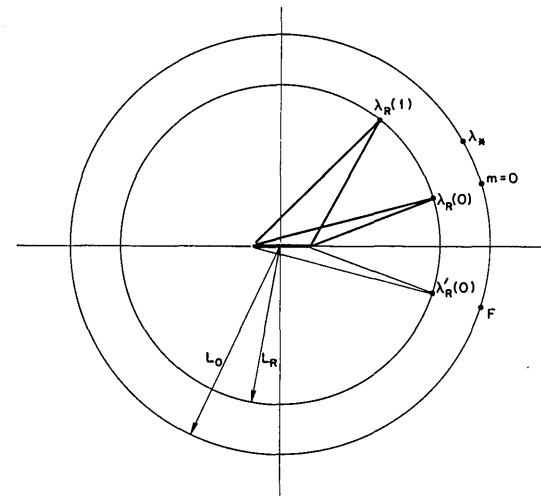

Fig. 7. Recording geometry for the Type V holographic grating. The outer circle includes the object point F, the zero-order image m, and the correction wavelength $\lambda*$. The inner circle passes through the two recording sources and the virtual recording source on the opposite side of the grating.

first (or possibly the second) requires the groove profiles to be sawtooth.[8] Except for some special recording geometries,[8,9] such profiles are not the natural result of a holographic ruling. However, the possibility of stigmatic or quasi-stigmatic groove patterns provided by holographic methods of fabrication deserves close attention, as other performance criteria (e.g., levels of stray light and ghosts)[9–11] may also be significantly improved in this manner.

It is conceivable to arrange our recording geometry to provide both the required imaging and blaze properties. To operate as an echelle, it is also possible to employ ion-etching techniques[12] to obtain the required groove profiles. Such techniques notwithstanding, a grating used in the $|m| = 1$ spectral order would in general not require an accurately controlled groove profile. While avenues which may permit the use of strong quasi-coherent x-ray or EUV sources to obtain $\lambda_R/\lambda* = 1$ are being investigated, we present here several schemes to scale the recording wavelength by the required factor of 10 or more into the regime of conventional lasers. In the case of $\lambda* \leqslant 100$ Å, such a scaling will also bring the recording wavelength into the regime of existing free-electron lasers ($\lambda_R \geqslant 1000$ Å).

One obvious procedure is to literally scale all linear dimensions by the ratio of recording wavelength to correction wavelength ($\lambda_R/\lambda*$). The large photoresist can then, in principle, be reduced by this same ratio, resulting in a flat grating surface with the required groove spacings. However, typically desired ruled widths are already quite large (100–500 mm), making the required scaled-up photoresists prohibitively large (several × 1000 mm).

We have found a procedure which allows the use of both conventional light sources and feasibly small photoresists. Figure 7 is a schematic diagram of the recording geometry, where the two point sources are relocated to provide quasi-stigmatism at $\lambda*$ for recording wavelengths λ_R which are significantly larger. In general, there are six free parameters which must be set—the three Cartesian coordinates for the two source points. Note that, due to the plane grating surface, both sources can be located on the same side of the grating, and thereby be simple real sources. The 2-D geometry of the in-plane mount immediately provides two constraints, leaving only two pairs of coordinates within the plane of dispersion. We anticipate the generation of hyperbolic groove patterns and therefore require the central groove ($x = 0$) to be straight. This requires that the source points be located on a circle centered at the grating center, removing another free parameter. We require the recorded line spacings to exactly match the stigmatic line spacings [Eq. (1)] at two points, x_1 and x_2, which provide these two clamping points along the grating aperture. The remaining parameter is the graze angle of incidence for one of the recording sources. We find the results to be relatively insensitive to this angle, but best results are found when the graze angles are small. For definitiveness, we place the reference source along the line joining the stigmatic $m = 0$ point and the grating center. Numerical solutions to the above constraints result in recording sources placed on circles of smaller radii than the distance L_0 to the $\lambda*$ and $m = 0$ focal surface images. The recording radius, L_R, is found to decrease linearly with $\lambda_R/\lambda*$ and quadratically with the mean graze angle α_0 of the $m = 0$ point. In the limit of a vanishingly small ruled width, we find

$$L_R/L_0 = 1 - \tfrac{1}{4}[(\beta/\alpha)^2 - 1]\alpha_0^2(\lambda_R/\lambda* - 1). \quad (15)$$

We find a minimum radius L_R below which the constraints outlined above cannot be simultaneously met. In the limit as the ruled width $\pm x/L_0$ vanishes, we find $(L_R/L_0)_{\min} = 1/2$ and is 0.54 for $x/L_0 = \pm 0.1$. Using Eq. (15), this results in a maximum value for the recording

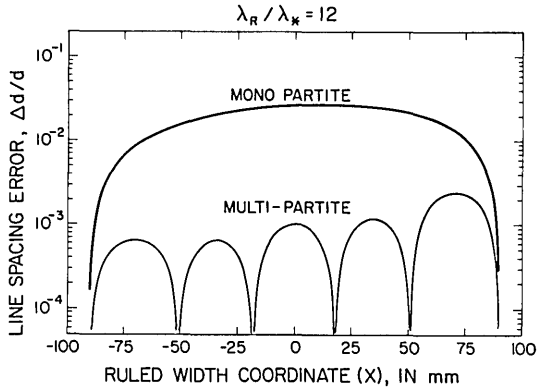

Fig. 8. Aberrations of the Type V grating as a function of distance along a 1-D section of the grating pupil ($y = 0$). A recording wavelength of $\lambda_R = 3637$ Å was simulated and the ray traces were performed at $\lambda* = 304$ Å. The fractional errors in the line spacing are indicated for both a single recording and a multipartite recording. The attainable resolution $\lambda/\Delta\lambda$ equals $d/\Delta d$.

wavelength. For example, at $\alpha_0 = 6°$ one can use $\lambda_R/\lambda*$ as large as 62 if $\beta/\alpha = 2$.

A good estimate to the aberrations induced at $\lambda*$ by this method is derived from the error in line spacing along the x axis. Figure 8 shows the simulated result of a $\lambda_R = 3637$ Å fabrication of the 180-mm ruled width medium wavelength EUVE flight grating, where $\lambda* = 304$ Å ($\lambda_R/\lambda* \simeq 12$). The line spacings are corrected precisely at ±90 mm, and the error in line spacing Δd at the grating center causes a spectral aberration $\Delta\lambda/\lambda = \Delta d/d$ of ~2.5%. By separately optimizing for five sections along the ruled width, this error decreases by a factor of 25, as shown by the bottom curves. The 3-D ray trace results of Fig. 6(c) compare well with those of Fig. 6(a) for straight mechanically ruled grooves. A factor of 2 further optimization is seen to be possible from Fig. 8, by adjusting the width of each section to provide uniform errors in spacing. For $\beta/\alpha = 2$, we find the following relation:

$$\lambda*/\Delta\lambda* = f_x^2/(\lambda_R/\lambda* - 1), \tag{16}$$

where f_x is the focal number of the incident light beam (the reciprocal of the cone angle converging to $m = 0$), and the correction points are optimally located at both edges of the exposed ruled width. Note that for large $\lambda_R/\lambda*$, Eq. (16) reveals that $\Delta\lambda* = \lambda_R/f_x^2$, i.e., independent of the wavelength. Thus, a grating or grating section which intercepts a 0.2° beam represents $f_x \simeq 290$ and if fabricated at $\lambda_R = 3637$ Å will deliver a resolution of $\Delta\lambda \simeq 0.04$ Å. At $\lambda = 1000$ Å, this represents $\lambda/\Delta\lambda = 25{,}000$.

The grating design class discussed in this paper (both in-plane and off-plane solutions) is defined by the unique imaging properties at grazing incidence of these plane gratings in converging light. Given the above procedure for fabrication of quasi-stigmatic versions by use of standard holographic methods, we designate this general class of grating designs as Type V. Types I–IV have been previously defined,[13] being curved gratings which generally intercept diverging light.

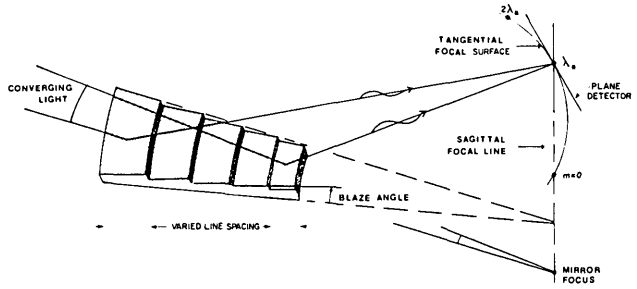

Fig. 9. Three-dimensional perspective of a concentric groove grating.

2. *Mechanical Ruling*

In principle, it is possible to mechanically fabricate the hyperbolic groove patterns discussed above. However, a concentric groove pattern would simplify the ruling,[14] as it provides a mechanical constraint along the radius of the grooves. Figure 9 shows a 3-D perspective of such a design. As the spacings between these concentric grooves can be adjusted to provide a point image at one wavelength $\lambda*$ along the axis of rotation of the grooves, stigmatism is available at this point. The ray trace results of Fig. 6(d) are virtually identical to those of the general hyperbolic grooves shown in Fig. 6(b). Thus, the constraint which facilitates mechanical ruling does not compromise performance.

The only difference appears to be slightly more astigmatism for the concentric grooves at the edges of the spectral field, due to the sagittal and tangential focal surfaces being more disparate for concentric grooves. The sagittal focal surface for this case is a line coincident with the symmetry axis of the grooves, for which the spectral images have zero height (normal to dispersion) at any wavelength. This results from the constant path-length difference along any one groove. Three-dimensional ray traces have confirmed this prediction. Calculations of the resulting aberrations in $\Delta\lambda$ proceed as per Sec. II.A.2, using Eq. (9) and the following relations:

$$L' = \sqrt{(L_0\cos\alpha_0 - x)^2 + L_0^2\cos^2\alpha_0\tan^2\beta}, \tag{17a}$$

$$L'* = \sqrt{(L_0\cos\alpha_0 - x)^2 + L_0^2\cos^2\alpha_0\tan^2\beta_0}, \tag{17b}$$

$$mN\lambda* = \sqrt{(L_0\cos\alpha_0 - x)^2 + L_0\sin^2\alpha_0} - \sqrt{(L_0\cos\alpha_0 - x)^2 + L_0^2\cos^2\alpha_0\tan^2\beta_0} - P_0, \tag{17c}$$

where $P_0 = L_0(1 - \cos\alpha_0/\cos\beta_0)$ is a scalar. After considerable algebraic manipulations, we find

$$\Delta = 3/2\,(m\lambda/d_0)[m(\lambda - \lambda*)/d_0]x^2, \tag{18a}$$

or

$$\lambda/\Delta\lambda = 1/3\,\alpha_0 f_x/|m(\lambda - \lambda*)|/d_0. \tag{18b}$$

Equation (18b) can also be written in a form[1] where d_0 is determined from the incident aspect uncertainty (see Sec. IV) and the desired resolving power, resulting in $(\lambda - \lambda*)/\lambda*$ being proportional to $(\lambda/\Delta\lambda)^{-2}$. To test

these predictions, ray traces were performed using parameters from a proposed design for the Advanced X-Ray Astrophysics Facility (AXAF). Figure 10(a) shows the result for the 10–30-Å band, where $\alpha_0 = 2.00°$, $f_x = 38.2$, $\lambda* = 20$ Å, $m = -1$, and $d_0 = 3550$ Å. The $|\lambda - \lambda*|^{-1}$ dependence of the resolving power is confirmed, as well as the magnitude of the proportionality constant in Eq. (18b).

However, the (tangential) focal surface which minimizes the aberrations in $\Delta\lambda$ is tilted relative to the sagittal line so as to be nearly normal to the diffracted beam, as indicated in Fig. 9. To further minimize the wavelength aberrations, a spherical detector is passed through the loci of smallest spot size for $\lambda*/2$ and $3/2\lambda*$. The optimum detector radii of curvature are plotted as solid curves in Fig. 5 for various limits. In our case, Fig. 10(a) confirms this optimization where a radius of 0.44 L_0 is used. The image widths $\Delta\lambda$ are significantly less than those using the sagittal detector but are still symmetric and asymptotic about $\lambda*$. The FWHM of these images is smaller than the extremum extents plotted here, resulting in slightly higher resolution, $\sim 4 \times 10^3$ over a factor of 2 in wavelength centered at $\lambda*$. As shown in Fig. 10(b), the image heights are small but nonzero along this curved surface, which is not coincident with the groove axis of rotation. Ray trace results are also shown for a flat detector passing through the stigmatic point at $\lambda*$. A flat detector can also be made to provide the correction obtained at any two wavelengths along the tangential surface by defocusing the $\lambda*$ image.

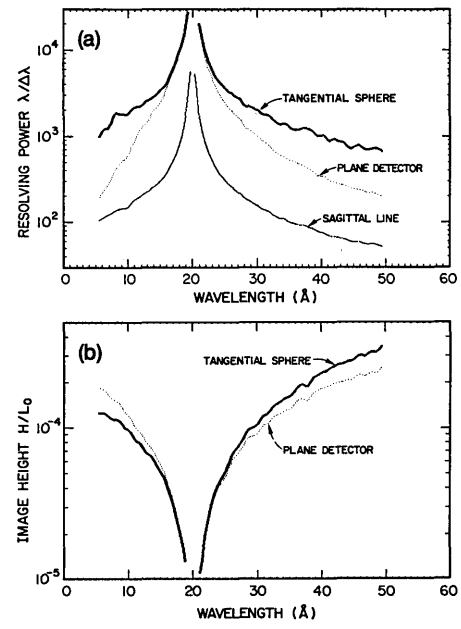

Fig. 10. Curves of extremum aberrations in wavelength and image height as functions of wavelength for the concentric groove grating specified in the text. Stigmatism is enforced at $\lambda* = 20$ Å. For the sagittal focal line, the image height is identically zero for all wavelengths.

C. Off-Plane Straight Fan Grooves

Figure 11 shows the projection of our off-plane grating solution on an orthogonal coordinate system. The x axis is coincident with the central ruling; the y axis is perpendicular to this ruling and also lies within the grating plane; and the z axis is perpendicular to this plane. In Fig. 11(c) the dispersion cone is shown in the y-z plane; this cross section also reveals blazed groove profiles for this conical diffraction mount.

1. *Imaging at a Correction Wavelength*

We again employ the aberrant light-path function given in Eq. (3). The path-length terms can be written as

$$L = \sqrt{(L_0 \cos\gamma_0 - x)^2 + [y + y(\lambda*)]^2 + [z(\lambda*)]^2}, \quad (19a)$$

$$L'* = \sqrt{(L_0 \cos\gamma_0 - x)^2 + [y - y(\lambda*)]^2 + [z(\lambda*)]^2}. \quad (19b)$$

At a given dispersion, optimal imaging at $\lambda*$ results from imposing the highest degree of symmetry. For the adopted grating geometry, there is planar symmetry about the x-z plane, so the chosen focal position of the correction wavelength $\lambda*$ is consistent with this symmetry, as shown in Fig. 11(b). This wavelength and $m = 0$ are placed equidistant from the x-z plane and thus are also equidistant from the central groove ($y = 0$). This choice also allows the diffraction efficiency to be blazed at an absolute maximum (100% of the reflectance) at $\lambda*$ for the central groove. The focal plane coordinates of $\lambda*$ are then

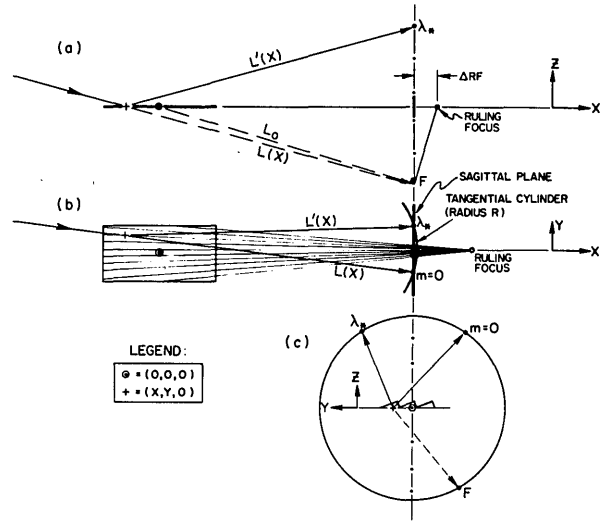

Fig. 11. Off-plane coordinate system. Projections are shown for the (a) plane containing the central groove, (b) grating plane, and (c) focal plane. Within the focal plane projection is also shown a groove profile geometry which maximizes efficiency at $\lambda*$.

$$y(\lambda*) = L_0 m\lambda*/(2d_0); \quad (20)$$

$$z(\lambda*) = L_0 \sin\gamma_0 \sqrt{1 - 1/4\ (m\lambda*/d_0/\sin\gamma_0)^2}\,. \quad (21)$$

In units of L_0,

$$L = \sqrt{1 - 2x\cos\gamma_0 + x^2 + (m\lambda*/d_0)y + y^2}, \quad (22a)$$

$$L'* = \sqrt{1 - 2x\cos\gamma_0 + x^2 - (m\lambda*/d_0)y + y^2}. \quad (22b)$$

Expanding the radicals and simplifying, we have the path-length difference

Table I. Aberration Coefficients for Off-Plane Solutions

	UNIFORM LINE SPACING $d(x,y)=d_o$	RADIAL GROOVES $\Delta RF = 0$ $d(r,\theta)=d(r)$	FAN GROOVES $\Delta RF=L_o\sin^2\gamma_o/\cos\gamma_o$ $d(r,\theta)=d(r)$	EQUAL CHORD FAN GROOVES $\Delta RF=L_o\sin^2\gamma_o/\cos\gamma_o$ $d(x,y)=d(x)$	VARIED ANGLE FAN GROOVES $\Delta RF=L_o\sin^2\gamma_o/\cos\gamma_o$ $d(r,\theta)=d(r)\cdot[1+\theta^2/2]$
terms in y					
a_{01}	-1	-1	-1	-1	-1
b_{01}	$+1$	$+1$	1	1	1
terms in xy					
a_{11}	$-1+(1/2)\gamma_o^2-(1/24)\gamma_o^4$	$-1+(1/2)\gamma_o^2-(1/24)\gamma_o^4$	$-1+(1/2)\gamma_o^2-(1/24)\gamma_o^4$	$-1+(1/2)\gamma_o^2-(1/24)\gamma_o^4$	$-1+(1/2)\gamma_o^2-(1/24)\gamma_o^4$
b_{11}	0	$1+(1/2)\gamma_o^2+(5/24)\gamma_o^4$	$1-(1/2)\gamma_o^2+(1/24)\gamma_o^4$	$1-(1/2)\gamma_o^2+(1/24)\gamma_o^4$	$1-(1/2)\gamma_o^2+(1/24)\gamma_o^4$
terms in x^2y					
a_{21}	$-1+(3/2)\gamma_o^2-(1/2)\gamma_o^4$	$-1+(3/2)\gamma_o^2-(1/2)\gamma_o^4$	$-1+(3/2)\gamma_o^2-(1/2)\gamma_o^4$	$-1+(3/2)\gamma_o^2-(1/2)\gamma_o^4$	$-1+(3/2)\gamma_o^2-(1/2)\gamma_o^4$
b_{21}	0	$1+\gamma_o^2+(2/3)\gamma_o^4$	$1-\gamma_o^2+(2/3)\gamma_o^4$	$1-\gamma_o^2+(2/3)\gamma_o^4$	$1-\gamma_o^2+(2/3)\gamma_o^4$
terms in y^3					
a_{03}	$1/2-(1/8)(m\lambda*/d_o)^2$	$1/2-(1/8)(m\lambda*/d_o)^2$	$1/2-(1/8)(m\lambda*/d_o)^2$	$1/2-(1/8)(m\lambda*/d_o)^2$	$1/2-(1/8)(m\lambda*/d_o)^2$
b_{03}	0	$-1/3-(1/3)\gamma_o^2-(2/9)\gamma_o^4$	$-1/3+(1/3)\gamma_o^2$	0	$-1/2+(1/2)\gamma_o^2$
c_{01}	0	0	0	0	0
c_{11}	$-1+0(2)$	$\gamma_o^2+(1/6)\gamma_o^4+0(6)$	$0(6)$	$0(6)$	$0(6)$
c_{21}	$-1+0(2)$	$(5/2)\gamma_o^2+0(4)$	$\gamma_o^2/2+0(4)$	$\gamma_o^2/2+0(4)$	$\gamma_o^2/2+0(4)$
c_{03}	$1/2+0(2)$	$1/6-(1/3)\gamma_o^2-(1/8)(m\lambda*/d_o)^2$	$1/6+(2/3)\gamma_o^2-(1/8)(m\lambda*/d_o)^2$	$1/2-(1/8)(m\lambda*/d_o)^2$	$\gamma_o^2/2-(1/8)(m\lambda*/d_o)^2$

$$L'* - L = (m\lambda*/d_0)[-y - xy\cos\gamma_0 + 1/2\,(1 - 3\cos^2\gamma_0)x^2y + 1/8\,(4 - m^2\lambda*^2/d_0^2)y^3 - x^3y + 3/2\,xy^3 - x^4y + 3x^2y^3 - 3/8y^5 + \ldots]. \quad (23)$$

We truncate this series to read

$$L'* - L = (m\lambda*/d_0)\sum a_{ij}x^iy^j, \quad (24)$$

where the coefficients a_{ij} are listed in Table I.

The light-path function of Eq. (3) also includes the interference term $mN\lambda$, which depends on the chosen groove pattern. For a conventional grating, the groove number N is simply equal to y/d_0, where d_0 is the uniform groove spacing. This cancels the leading term in the path length from Eq. (23), however does not correct for the first-order focusing term in xy. The resulting attainable resolving power is very low,[15]

$$\lambda/\Delta\lambda = \sin\gamma_0/(\sin\gamma_{max} - \sin\gamma_{min}), \quad (25)$$

where γ is the graze angle of reflection. This aberration is a result of different distances between the focal surface and each dispersion point on the grating. However, by using a second such grating in tandem,[15] as illustrated in Fig. 12(a), a nearly constant ray path distance is maintained through the system. In this way, $\lambda/\Delta\lambda$ can be increased by typically a factor of 10–20. Figure 12(b) shows an example ray trace, revealing highly astigmatic images, and an image curvature which appears to be the limiting effect on the wavelength resolution.

For the extreme off-plane mount in converging light, linear dispersion per unit wavelength is proportional to L/d, where L varies across the grating pupil and is responsible for the aberrations described above. Rather than using a second grating to largely remove variations in the numerator of this ratio, one can maintain a constant dispersion by varying the denominator d in the same manner as L passively varies across the aperture. This motivates the basic groove pattern illustrated in Fig. 11(b), where the spacings increase in proportion to L further from focus. Thus, the variation in groove spacings is in the direction along each groove, rather than in the direction of the ruled width.

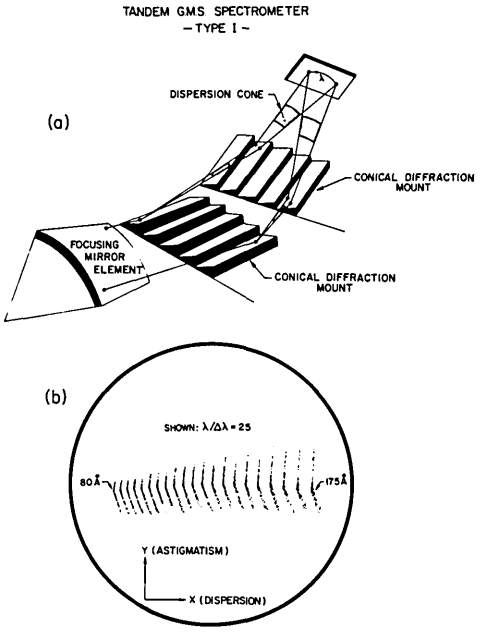

Fig. 12. Tandem gratings, each having conventional uniform line spacing: (a) 3-D perspective, (b) an example ray trace for extreme UV spectroscopy revealing a spectral resolution in the $\lambda/\Delta\lambda$ = 100–200 range.

To simplify a mechanical ruling of this type of design, we constrain the grooves to be straight and to converge to a common point, the ruling focus. Stigmatic interference fringes, generated by hypothetical coherent sources $\lambda*$ at the focal positions of $\lambda*$ and $\lambda = 0$, are hyperboloids of revolution colliding with the plane grating surface. In the limit as $\gamma \to 0$ and as the grating is infinitely far from focus ($L \to \infty$), the fringes are hyperbola asymptotes coincident with straight grooves which intersect in the focal plane containing $\lambda*$ and $\lambda = 0$. However, near the intersection point this approximation clearly fails, as the path-length difference to the sources would be equal (zero) for all grooves, and thereby provides no constructive interference for $m \neq 0$. Rather, for finite values of γ and L, a more accurate approximation is obtained by making the (straight) grooves tangent to the optimal curved grooves at the grating center. In this case, the grooves become more parallel and thereby intersect behind the plane containing the source points. In determining the groove number N, we therefore consider a displacement, ΔRF, of the ruling focus behind this focal plane. We adopt a polar coordinate system, where $\theta = \arctan[y/(L_0 \cos\gamma_0 - x + \Delta RF)]$ and $r^2 = (L_0 \cos\gamma_0 - x + \Delta RF)^2 + y^2$. For grooves which fan-out linearly from a common point, $d(r,0)/d_0 = r/[L_0 \cos\gamma_0 + \Delta RF]$. For equal angular spacings between grooves, $d(r,\theta) = d(r,0)$, the groove number is $N = r\theta/d(r,0)$ or

$$N = [(L_0 \cos\gamma_0 + \Delta RF)/d_0] \arctan[y/(L_0 \cos\gamma_0 - x + \Delta RF)]. \tag{26}$$

Expanding the trigonometric functions and treating the graze angle γ as a small quantity, we determine coefficients b_{ij}, corresponding to the powers of x and y given in Eq. (24), to be

$$\begin{aligned}
b_{01} &= +1, \\
b_{11} &= (1 + 1/2\,\gamma_0^2 + 5/24\,\gamma_0^4 + \ldots) \\
&\quad - \Delta RF(1 - 1/2\,\gamma_0^2 + \ldots) + \Delta RF^2 + \ldots, \\
b_{21} &= (1 + \gamma_0^2 + 2/3\,\gamma_0^4 + \ldots) - \Delta RF(2 + 3\gamma_0^2 + \ldots) \\
&\quad + 3\Delta RF^2 + \ldots, \\
b_{03} &= (-1/3 - 1/3\,\gamma_0^2 - 2/9\,\gamma_0^4 + \ldots) \\
&\quad + \Delta RF(2/3 + \gamma_0^2 + \ldots) - \Delta RF^2 + \ldots, \\
b_{13} &= -1 - 3/2\,\gamma_0^2 + 3\Delta RF - 6\Delta RF^2 + \ldots, \\
b_{31} &= +1 + 3/2\,\gamma_0^2 - 3\Delta RF + 6\Delta RF^2 + \ldots, \\
b_{23} &= -2 + 8\Delta RF + \ldots, \\
b_{41} &= +1 - 4\Delta RF + \ldots.
\end{aligned} \tag{27}$$

In all cases $c_{01} = 0$, as with uniform line spacings. However, cancellation of the other dominant terms depends strongly on the choice of ΔRF. Defining $\Delta = (m\lambda*/d_0) \sum c_{ij} x^i y^j$, where $c_{ij} = a_{ij} + b_{ij}$, several solutions for ΔRF can be interpreted:

Case a: $\Delta RF = 0$

This solution has been proposed as a radial groove grating[6] for which the central hub of the rulings (analogous to the ruling focus) lies in the plane of the zero-order image (compare Fig. 6 of Ref. 6). While one can also consider curving the focal surface, as investigated in the next section, this reduces aberrations only away from $\lambda*$ (if only the focal surface was displaced, the symmetry would be disturbed and result in larger aberrations). The aberration coefficients are given in Table I, with dominant terms being

$$\Delta = (m\lambda*/d_0)[\gamma_0^2 xy + 5/2\,\gamma_0^2 x^2 y + 1/6\,y^3 + \ldots] \cdot \tag{28}$$

Using the off-plane analogs of Eqs. (6a) and (6b),

$$\lambda/\Delta\lambda = (m\lambda*/d_0)/(\delta\Delta/\delta y), \tag{29a}$$

$$H/L_0 = (1/\gamma_0)(\delta\Delta/\delta x), \tag{29b}$$

we have the focal plane aberrations:

$$\lambda/\Delta\lambda \simeq [\gamma_0 f_x^{-1} + 5/8\,f_x^{-2} + 1/8\,f_y^{-2}]^{-1}, \tag{30a}$$

$$H/L_0 \simeq (m\lambda*/d_0)(\gamma_0 + 5/2\,f_x^{-1}) \Big/ f_y, \tag{30b}$$

where $f_x \equiv 1/(\gamma_{\max} - \gamma_{\min})$. The linear dependence on γ_0 dominates both aberrations and results in the reported degradation of imaging as the graze angle becomes large.[6] Ray traces of this solution are presented in Fig. 13(d), confirming the above quantitative predictions. The parameters used in this ray trace correspond to those used in the in-plane straight groove ray traces of Fig. 3:

$$\gamma_0 = 7.089°; \quad L_0 = 485.47 \text{ mm}; \quad d_0 = 2125 \text{ Å};$$
$$\gamma_{\min} = 6.02°; \quad \gamma_{\max} = 8.62°; \quad f_y = 6.2; \quad \lambda* = 150 \text{ Å}.$$

Case b: $\Delta RF \simeq L_0 \sin^2\gamma_0$

This solution, an oriental fan, was introduced in our previous paper.[1] If $\Delta RF/L_0 = \sin^2\gamma_0 \cos\gamma_0$, the dominant term c_{11} of the light-path function decreases by a factor γ_0^4 compared to uniform line spacings, and a factor γ_0^2 in comparison to the radial groove solution. Although this already causes the term to be negligible at grazing incidence, Eqs. (27) also reveal that a slight alteration, where $\Delta RF/L_0 = \sin\gamma_0 \tan\gamma_0$, reduces the proportionality constant to γ_0^6, allowing the design to be extended to large graze angles. In either case, the dominant terms are given in Table I as

$$\Delta = (m\lambda*/d_0)[1/2\,\gamma_0^2 x^2 y + 1/6\,y^3 + 1/2 xy^3 + \ldots] \cdot \tag{31}$$

This is the result reported previously,[1] resulting in focal plane aberrations:

$$\lambda/\Delta\lambda \simeq [1/8\,f_x^{-2} + 1/8\,f_y^{-2}]^{-1} \equiv 8f^2,$$
$$\text{where } f \equiv 1/\sqrt{f_x^{-2} + f_y^{-2}}, \tag{32a}$$

$$H/L_0 \simeq (1/2)\,(m\lambda*/d_0)/(f_x f_y). \tag{32b}$$

Note that $\lambda/\Delta\lambda$ and H/L_0 are both independent of the graze angle. The optimal displacement, ΔRF, can also be obtained by minimizing the variation in $L(x,0)/d(x,0)$ across the grating pupil coordinate x, as suggested above. Writing $L(x,0) = \sqrt{(L_0 \cos\gamma_0 - x)^2 + L_0^2 \sin^2\gamma_0}$, using $d(x,0)/d_0$ as given from the derivation of Eq. (26), and setting $\delta(L/x)/\delta x = 0$, we find

$$(L_0 \cos\gamma_0 - x)^2 + L_0^2 \sin^2\gamma_0 = (L_0 \cos\gamma_0 - x) \times (L_0 \cos\gamma_0 - x + \Delta RF), \tag{33}$$

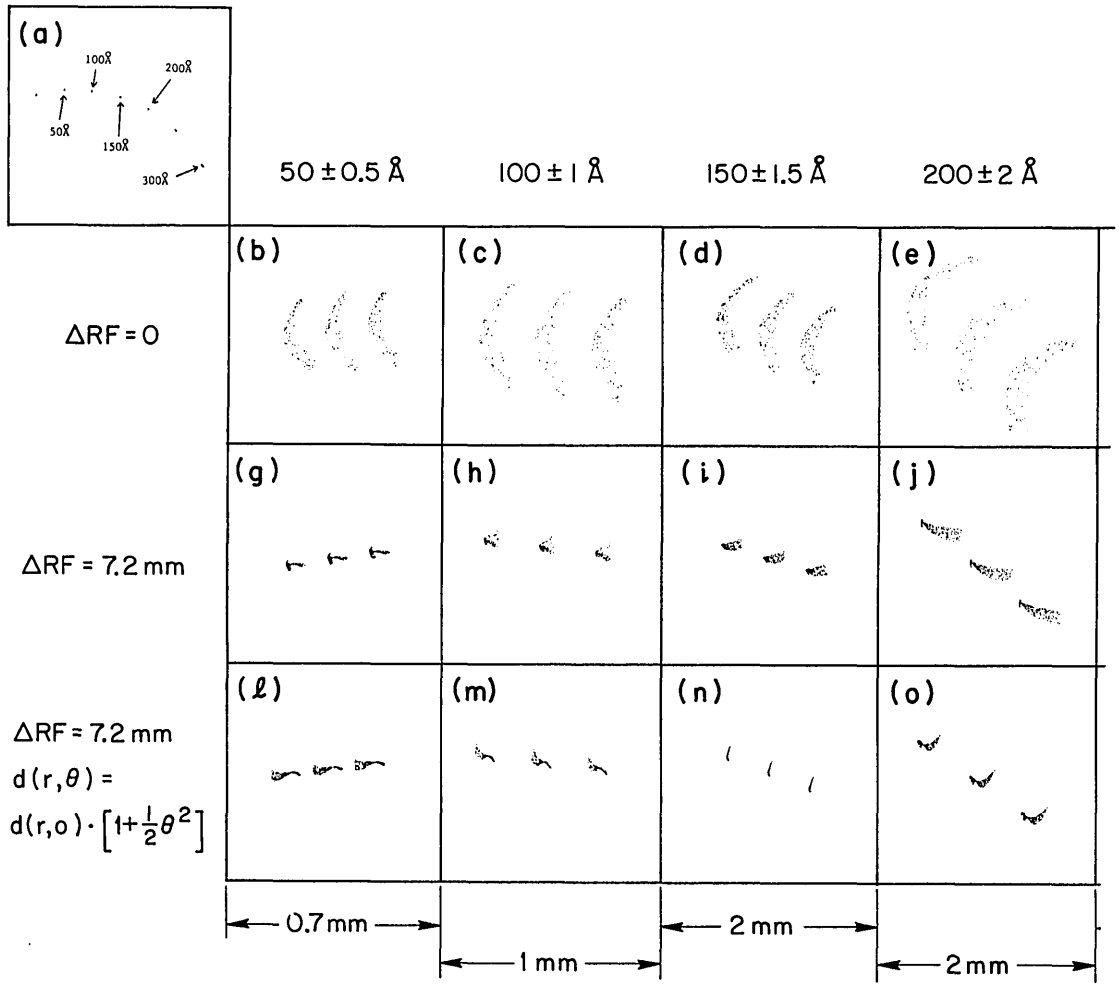

Fig. 13. Ray traces for oriental fan grating showing (a) the conical wavelength map and the spot diagrams for various cases: (b)–(f) no displacement of the ruling focus behind the mirror focus $\Delta RF = 0$; (g)–(k) an optimal displacement $\Delta RF \simeq L_0 \sin\gamma_0^2$; and (l)–(p) an optimal displacement plus an optimized angular variation of the groove spacings. In all cases the sagittal detector plane has been employed.

for which the solution is $\Delta RF/L_0 = \sin\gamma_0 \tan\gamma_0$, as derived above by minimizing the error in the light-path function. Figure 11(a) shows a geometric operational definition of ΔRF, being that from a right triangle with one leg equal to L_0. Thus F lies on a semicircle.

A comparison of Eqs. (30a) and (32a) reveals that this displacement of the ruling focus behind the zero-order image significantly reduces the wavelength aberrations. In the limit as γ_0 vanishes and $f_x \ll f_y$, the reduction is a factor of 5. At finite graze angles, the first-order focusing term of the case $\Delta RF = 0$ also contributes, resulting in even larger differences. In the limit as $f_x \gg \max(f_y, 8\gamma_0 f_y^2)$, the aberrations in $\Delta\lambda$ are equal for the two cases. The image heights [Eqs. (30b) and (32b)] are reduced at least a factor of 5, as $\gamma_0 \to 0$. For $\gamma_0 > 5/(2f_x)$, the astigmatic term c_{11} dominates in the case $\Delta RF = 0$, leading to larger differences. Figure 13(i) shows the results given the same (EUVE) parameters used for Case a, revealing an enhancement in spectral resolution and a factor of 10 reduction in astigmatism. Also evident in these spot diagrams are central cores which are significantly smaller than the extremum ray envelopes.

Comparison of Eqs. (8b) and (32b) or Fig. 13 reveals that the image height is significantly smaller than that of the in-plane solution, by a factor of α_0. However, for the in-plane solution, straight grooves yield a $\lambda/\Delta\lambda$ which depends only on the focal number along the direction of the groove lengths, f_y, because the spacings of the in-plane grooves are varied to obtain perfect focusing along an axis running across the ruled width. In contrast, the off-plane grating was assumed to have equal angular spacings, for which perfect focusing is not achieved across any slice of the ruled width. Therefore, $\lambda/\Delta\lambda$ for the off-plane solution depends on the focal numbers in both directions (f_x is along the groove lengths and f_y is across the ruled width for the off-plane geometry). If both focal numbers are equal, the resolving power of the off-plane solution is a factor of 2 lower than for the in-plane solution. Since the variation in reflection angle across the grating aperture is minimized by choosing $f_x > f_y$, the spectral resolution is dominated by f_y.

2. *Optimized Angular Variation of Fan Grooves*

The spectral resolution can be significantly improved by relaxing the constraint of equal angular spacings, i.e., not requiring that $d(r,\theta) = d(r,0)$. We seek to cancel the dominant aberration along the y axis and to thereby obtain $c_{03} \simeq 0$. We anticipate a functional dependence $d(r,\theta) = d(r,0) \times (1 + \eta\theta^2)$, for which the groove number N is a modified version of Eq. (26):

$$N = (L_0 \cos\gamma_0 + \Delta RF)/d_0 \int_0^\theta d\theta/(1 + \eta\theta^2). \tag{34}$$

Performing the integral and substituting $\Delta RF = \sin\gamma_0 \tan\gamma_0$, we have

$$\begin{aligned} N &= (L_0 \cos\gamma_0 + \Delta RF)/d_0 \times (\theta - \eta\theta^3/3 + \eta^2\theta^5/5 + \ldots) \\ &\simeq N(\eta = 0) - (\eta/3)L_0/d_0 \\ &\quad \times \arctan^3[y/(L_0 \cos\gamma_0 - x + \Delta RF)]. \end{aligned} \tag{35}$$

If $\eta = 1/2$, the additional term of Eq. (35) cancels the dominant terms in c_{03}, c_{13}, and c_{23}, as evident from inspection of Eqs. (23), (27), and (31). This provides the desired result, namely, $\lambda/\Delta\lambda \simeq 8f_x^2$ independent of f_y. A significant increase in $\lambda/\Delta\lambda$ is shown in the ray traces of Fig. 13(n). Also apparent from Eqs. (35) and (31) is that a choice $\eta = -1$ results in a factor of 3 increase in the c_{03} term and thus in the spectral aberration compared to the previous case. These angular spacings of the grooves are approximately such that the linear spacings are independent of y, i.e., $d(x,y) = d(x)$. Since this corresponds to equal intervals between grooves of the quantity $\tan\theta$, the term θ =arctan [. . .] in Eq. (26) is revised to read simply $\theta = y/(L_0 \cos\gamma_0 - x + \Delta RF)$.

For values of $(m\lambda*/d_0)^2$ which are non-negligible, one must also consider the contribution of that term from a_{03}, which is $(\lambda/\Delta\lambda) \simeq (32/3)f_y^2/(m\lambda*/d_0)^2$. By a minor adjustment of the value $\eta = 1/2 - 3/8(m\lambda*/d_0)^2$, this term can be minimized to equal $\lambda/\Delta\lambda \simeq 32/9f_y^2 f_x \gamma_0/(m\lambda*/d_0)^2$. If $\lambda*$ is the blazed wavelength, it is also noted that $m\lambda*/d_0 = 2\sin\delta \sin\gamma_0$, where δ is the blaze angle of the grating grooves. Thus, such an adjustment in η is necessary only if both the graze angle and the blaze angle are large.

3. *Spectral Field Aberrations*

As for the in-plane solution, we again consider the growth in aberrations as one moves in wavelength away from $\lambda*$. A convenient focal surface for this analytic calculation is the plane containing both $\lambda*$ and $\lambda = 0$ and being perpendicular to the x axis (the central groove). We will find this to be the sagittal surface, where the image heights are minimized, analogous to the sagittal sphere for the in-plane grating. We again write for the difference in wave front aberration, $\Delta - \Delta* = L' - L'* + mN(\lambda - \lambda*)$. In the present geometry, we substitute the following:

$$L' = \sqrt{1 - 2x\cos\gamma_0 + x^2 - (m\lambda*/d_0)y + y^2 + 2[m(\lambda* - \lambda)/d_0]y}, \tag{36a}$$

$$L'* = \sqrt{1 - 2x\cos\gamma_0 + x^2 - (m\lambda*/d_0)y + y^2}, \tag{36b}$$

$$\begin{aligned} N &= (1/d_0)[y + (1 - \gamma_0^2/2)xy \\ &\quad + (1 - \gamma_0^2)x^2y - (1/3 - \gamma_0^2)y^3 + \ldots], \end{aligned} \tag{36c}$$

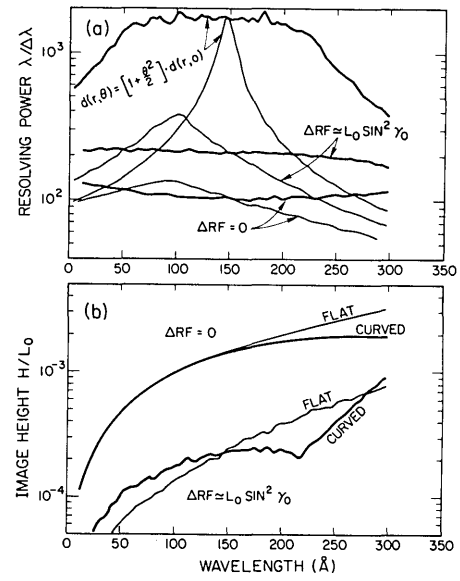

Fig. 14. Curves of extremum aberrations in wavelength and image height as functions of wavelength for the off-plane grating specified in the text. The correction wavelength is 150 Å. The light curves summarize the results of Fig. 13 for the sagittal focal plane, while the dark curves indicate the ray trace results for the optimally curved cylinders.

where we have substituted for $y(\lambda) = y(\lambda*) + L_0 m(\lambda - \lambda*)/d_0 = L_0 m(\lambda - \lambda*/2)/d_0$, for $z^2(\lambda) = L_0^2 \sin^2\gamma_0 - y^2(\lambda)$, and where the value for N has been taken from Table I for equal angular spacings. Expanding the radicals, we find

$$\begin{aligned} \Delta - \Delta* &= [1/2 \cos\gamma_0 m(\lambda - \lambda*)/d_0 \, m\lambda/d_0]x \\ &\quad + [1/2 \, m(\lambda - \lambda*)/d_0 \sin^2\gamma_0]x^2y \\ &\quad - [1/2 \, m(\lambda - \lambda*)/d_0 \, m\lambda/d_0]y^2 \\ &\quad + [1/6 \, m(\lambda - \lambda*)/d_0]y^3. \end{aligned} \tag{37}$$

The terms in x^2y and in y^3 are identical to those present in $\Delta*$ and therefore represent the same value of $\lambda/\Delta\lambda$ as well as the previous result for H/L_0, where λ now replaces $\lambda*$. However, there are two additional terms for $\lambda \neq \lambda*$, one in x and one in y^2. The former gives rise to a shift in H/L_0 which grows as $(\lambda - \lambda*)\lambda$ and is significant only for large values of $(\lambda - \lambda*)$, signifying departure from a truly sagittal focal surface. The latter term represents a degradation in spectral resolution which grows linearly with $(\lambda - \lambda*)$. Taking $\delta\Delta/\delta y$, we thereby derive a resolution:

$$\lambda/\Delta\lambda \simeq 8/[f_x^{-2} + f_y^{-2} + 8|m|(\lambda - \lambda*)/d_0/f_y)]. \tag{38}$$

Note that this is identical to the spectral field obtained in Eq. (14a) for the in-plane straight groove solution, if the off-plane line spacing is decreased by a factor of α_0. In Sec. III, this is shown to represent equal dispersive power for the in-plane and off-plane mountings. Note that, for $\lambda < \lambda*$, the spectral field aberration partially cancels the first two terms in Eq. (38) and thereby maximum $\lambda/\Delta\lambda$ is obtained somewhat shortward of $\lambda*$. Figure 14 confirms this formula across the factor of 4 in spectral range which is shown, where $\lambda/\Delta\lambda$ peaks at $2\lambda*/3$, and decreases symmetrically to either side. Also

shown are the cases of varied angular spacings and the nonoptimal case of $\Delta RF = 0$. In these cases, the resolving power also degrades along this plane focal surface as λ moves away from $\lambda*$. This has a particularly deleterious effect on the varied angle design, whose resolution remains high only in the immediate vicinity of $\lambda*$.

To minimize aberrations in $\Delta\lambda$, we next consider curvature of the optimal tangential focal surface. If a detector displacement toward the grating, Δx_D, is inserted into the expansion of Eq. (22b) (i.e., $x = x + \Delta x_D$), an additional term is introduced into the aberrant light-path function:

$$\Delta = \Delta + (1/2)\,(\Delta x_D/L_0)y^2. \tag{39}$$

This cancels the y^2 term of the field aberration in Eq. (37) if $\Delta x_D/L_0 = -[m(\lambda* - \lambda)/d_0\, m\lambda/d_0]$. Note that this quantity is invariant on a substitution $\lambda = \lambda* - \lambda = \lambda*/2 - (\lambda - \lambda*/2)$. Thus, the detector curvature is symmetric about the x-z plane, which contains $\lambda*/2$. To minimize the number of adjustable parameters, we fit a cylinder through the focal plane positions of $\lambda*$ and $\lambda = 0$, as shown in Fig. 11(b). The center of curvature is therefore in the x-z plane, and a displacement toward the grating of this focal surface can be written as

$$\Delta x_D = R(\cos\phi - \cos\phi*), \tag{40}$$

where R is the radius of curvature of the cylinder, and where $\sin\phi \simeq y(\lambda)/R$. Using the substitution given above for $y(\lambda)$, the detector displacement can be expressed in terms of its radius and the impinging wavelength:

$$\Delta x_D/L_0 \simeq -(1/2)(m/d_0)^2\lambda(\lambda* - \lambda)L_0/R. \tag{41}$$

Matching this curvature with that derived above to cancel the dominant field aberration, the optimal radius is thus $R/L_0 \simeq 1/2$. Ray traces confirming this result are summarized in Fig. 14 for both equal and varied angle fan gratings. The resolution becomes nearly constant as a function of λ. Also shown is the result for the case $\Delta RF = 0$, for which the same radius of curvature has been reported by Cash.[6] However, we find the magnitude of the spectral resolution at $\lambda*$ for this geometry is still given by Eq. (30a). We do not find any significant increase in astigmatism using a tangential focal surface, as shown in Fig. 14(b).

III. Dispersive Aberrations

The net attainable resolution depends not only on the grating aberrations but also on the ability of the grating to dispersively separate the finite zero-order image sizes entering the grating or introduced downstream of the dispersion. Figure 15 illustrates the effect of a mirror focusing blur in the dispersion direction. If F is the effective focal length of the mirror and ε is the corresponding mirror quality (i.e., in radians of aspect uncertainty in the sky), a bundle of rays will impinge on the grating at deviant positions and angles. As the grating line spacing is also a function of position, there are three aberrant effects; however Fig. 15 indicates they may all be cast in terms of an effective angular error $\Delta\alpha$

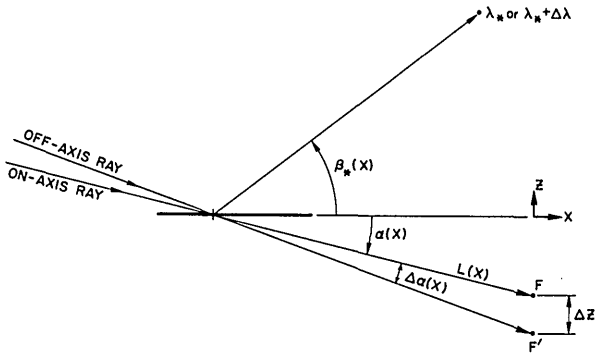

Fig. 15. Off-axis in-plane grating illumination, revealing the equivalent error in incident angle $\Delta\alpha_0$, produced by a displacement of the mirror focus from F to F'.

alone. For the present analysis, we may ignore variations in $\Delta\alpha$ across the grating pupil and write simply

$$\Delta\alpha_0 \simeq (F/L_0)\varepsilon. \tag{42}$$

A. In-Plane Diffraction

For the in-plane gratings, this error is converted directly into a wavelength aberration through a differential of the grating equation:

$$\Delta\lambda = (d_0/m) \times (\Delta\beta_0 \sin\beta_0 - \Delta\alpha_0 \sin\alpha_0). \tag{43}$$

We fix the diffracted angle β and thereby determine the uncertainty in λ at that focal plane position.

Equation (43) can be written in several forms. In terms of the plate scale, $\delta\lambda/\delta s$, we obtain $\Delta\lambda = F\varepsilon(\delta\lambda/\delta s)\sin\alpha_0/\sin\beta_0$, or in terms of dimensionless ratios, we find in the limit of small angles:

$$\Delta\lambda/\lambda = 2(F/L_0)\varepsilon/(|\beta_0^2/\alpha_0^2 - 1|\alpha_0). \tag{44a}$$

Thus, the dispersive resolving power of these spectrometers increases linearly with the system length ($\sim L_0$) and decreases linearly at smaller graze angles α. However, this decrease can be offset by using larger ratios of β/α and therefore use of an inside spectral order. For example, if $F/L_0 = 10$, $\varepsilon = 1$ sec of arc, $\alpha_0 = 5°$, and $\beta_0/\alpha_0 = 5$, one achieves $\lambda/\Delta\lambda = 20{,}000$. If operating at the blaze condition, the relative diffraction efficiency is approximately[16] equal to the ratio (α/β) for $m < 0$ and (β/α) for $m > 0$, and α can be expressed in terms of (β/α) and the facet graze angle γ. This yields

$$\Delta\lambda/\lambda = (F/L_0)\varepsilon/\sin\gamma_0/|\beta_0/\alpha_0 - 1|. \tag{44b}$$

Figure 16 plots this result as a function of γ_0, assuming $\beta_0/\alpha_0 = 3$, for various combinations of F/L_0 and ε. However, for $m = -1$ and peak blaze efficiencies of 50% or smaller, the curve of diffraction efficiency vs wavelength extends to wavelengths significantly larger than λ_{blaze}. In this way, significantly higher resolution can be achieved through large values of β longward of the blaze.

The required grating size is determined by f_y along the grooves and by f_x across the ruled width. The ruled width is almost always the larger dimension at grazing

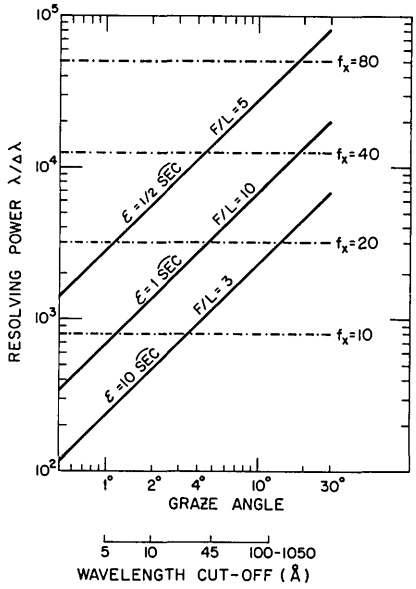

Fig. 16. Practically attainable spectral resolution for a grazing incidence grating in a converging beam as a function of the mean graze angle γ_0. L_0 is the distance from grating center to focus. Other parameters assumed for the grating mounting are indicated in the text. The solid lines indicate the ability to dispersively separate images from collecting mirrors (focal length F) of various image qualities (ε). The horizontal dot–dash lines indicate the grating aberrations for an optimized fan groove pattern having varied angular spacings. The wavelengths for which single-coating reflectance is 50% are indicated at the bottom.

incidence for this in-plane mount and is approximately equal to

$$\text{ruled width} \simeq [(L_0/f_x)/\sin\gamma_0](\beta_0/\alpha_0 + 1)/2. \quad (45)$$

B. Conical Diffraction

To obtain maximum efficiency, the blaze angle δ of the grating grooves is made equal to the incident and diffracted angles at the grating center. Thus, the correction wavelength $\lambda*$ is also the blazed wavelength. If ε represents the aspect uncertainty of the collecting mirror in the direction of dispersion, we find for the resolution

$$\Delta\lambda/\lambda = (F/L_0)\varepsilon/\tan\delta/\sin\gamma_0/2, \quad (46)$$

where γ_0 is the graze angle of reflection at the grating center. This result is similar to that obtained for conical gratings in parallel light, where (F/L_0) is then replaced by the concentration ratio of the collimating/collecting mirror system. To feasibly limit the grating size, we choose a blaze angle of 45°. Given equal reflection angles γ_0, this yields a dispersive resolution equal to that of an in-plane grating blazed at $\beta_0/\alpha_0 = 3$. This is evident from comparison of Eqs. (44b) and (46) and is plotted in Fig. 16.

Also plotted in Fig. 16 are the intrinsic aberrations for a varied angle fan grating, which depend on only the focal ratio f_x along the grooves. In the EUV ($\lambda \sim$ 100–1000 Å), graze angles less than ~12° must be used to obtain reflection efficiency in excess of 50%. This results in the dispersive and grating aberrations being comparable, limiting $\lambda/\Delta\lambda$ to values of ~7000, given $F/L_0 = 10$, $\varepsilon = 1$ sec of arc, and $f_x = 30$. If $F/L_0 = 5$, $\varepsilon = 0.5$ sec of arc, and $f_x = 60$, the resolution increases to $\lambda/\Delta\lambda \simeq 36{,}000$. At the shortest wavelengths where single layered reflection gratings are feasible ($\lambda \sim 10$ Å), dispersive aberrations limit the resolution. However, by use of grating multilayer coatings,[17] it may be possible to extend such designs to shorter wavelengths. This will also permit larger graze angles for coverage of narrow bands in the the soft x-ray region.

In the case of the off-plane mount, the long dimension of the grating is that along the groove lengths and depends on the focal ratios in both directions:

$$\text{groove length} \simeq (L_0/f_x)/\sin\gamma_0 + (L_0/f_y)\tan\delta/\sin\gamma_0. \quad (47)$$

Thus, for the usual case of $f_y < f_x$, the conical mount requires a longer grating. For example if $f_x = 2f_y$, the off-plane grating is ~50% larger in both dimensions.

The above analysis indicates the theoretical limit to resolution at small graze angles, independent of the spectral order. However, a very practical limitation is also the required line density. It appears not to be generally appreciated that the use of grazing incidence is only partly motivated (although necessarily so) by the high reflective throughput achieved at short wavelengths. A second motivation for grazing incidence is also crucial and applies only to in-plane diffraction. Dispersion increases by the factor $1/\sin\beta$, where β is the graze angle of diffraction for an in-plane mounting. This angle is of the order of γ = the graze angle, thereby providing the very high angular dispersion necessary to obtain a given $\lambda/\Delta\lambda$ at short wavelengths. At normal incidence or in conical diffraction, where this factor is absent, the required line densities are of the order of $1/\gamma$ larger or

$$1/d(\text{lines/mm}) = 50/\Delta\lambda(\text{Å}) \times \varepsilon(\text{sec of arc}) \times |F/L_0/m| \times \cos\delta. \quad (48)$$

For example, at $\delta = 45°$ and $F\varepsilon/L_0 = 10$, a resolution in first order of $\lambda/\Delta\lambda = 20{,}000$ at 100 Å requires 70,000 lines/mm, which is unfeasible by a factor of 10. Thus, high spectral orders must be used to obtain such resolutions, provided the graze angles are also made large enough to honor Eq. (46).

IV. Misalignment Aberrations

As shown above, either in-plane or off-plane gratings can attain high resolution performance. In this section, we consider aberrations induced by fixed errors in the positioning of the components of a spectrometer utilizing in-plane gratings. These may be separated into three categories: (1) positioning of the convergent beam focus relative to the grating, (2) linear and angular positioning of the grating relative to the imaging focus and the assumed spectral focus, and (3) positioning of the detector relative to the grating. Each of these, predominantly (1) and (2), will result mostly in a shift in wavelength, $\lambda = \lambda* + D\lambda$, which is diffracted to the point in space previously occupied by $\lambda*$. Variations in this shift, for different regions of the grating aperture,

result in a residual aberration $\Delta\lambda_M$ due to the misalignment.

Fixing the exit pupil at the position occupied by $\lambda*$ in Sec. II, one can set up a general if not elegant equation for the aberrant light path:

$$\Delta_M = L*' - L + mN\lambda*(1 + D\lambda/\lambda*) - \Delta*, \tag{49}$$

where the factor in parenthesis represents the fractional shift in wavelength being diffracted to the exit pupil. This shift is determined by requiring the coefficient of the x^1 term to vanish in the above expression. The value of the interference term $mN\lambda*$ is obtained from Eq. (4b), and the perturbed distances $L*'$ and L are given in dimensionless units of L_0:

$$L = \sqrt{(\cos\alpha_0 - x - \Delta x)^2 + (y + \Delta y)^2 + (\sin\alpha_0 + \Delta z)^2}, \tag{50a}$$

$$L*' = \sqrt{(\cos\beta_0 - x - \Delta x')^2 + (y + \Delta y')^2 + (\sin\beta_0 - \Delta z')^2} \tag{50b}$$

for the case $L_0 = L_0'$. For the concentric groove geometry, L is also described by Eq. (50a), but $L*'$ is obtained from a perturbed form of Eq. (17b):

$$L*' = \sqrt{(\cos\alpha_0 - x - \Delta x')^2 + (y + \Delta y')^2 + (\cos\alpha_0 \tan\beta_0 - \Delta z')^2}, \tag{51}$$

and the interference term $mN\lambda*$ is given in Eq. (17c).

Consider the mirror focus of Fig. 9 to be displaced by Δz_F along the rotation axis of the concentric grooves. In terms of the equivalent off-axis mirror angle Ω, $\Delta z_F = F\Omega_z$, where F is the effective mirror focal length. For the present analysis, the focal surface of the collecting mirror is assumed to include the groove axis of symmetry. The induced shift in wavelength diffracted to the fixed exit pupil can be obtained from Eq. (43) or Eq. (49):

$$D\lambda/\lambda \simeq 2(\Delta z_F/L_0)/\alpha_0/(\beta_0^2/\alpha_0^2 - 1). \tag{52}$$

The variation in this shift arises dominantly from the x^2 term of Eq. (49) and equals

$$\Delta\lambda/\lambda* \simeq (3/f_x)(\Delta z_F/L_0)[\beta_0^4/\alpha_0^4 + 2/3\,\beta_0^2/\alpha_0^2 - 5/3)/(\beta_0^2/\alpha_0^2 - 1)^2] \cdot \tag{53}$$

For $\beta_0/\alpha_0 > 2$, the bracketed term is approximately equal to unity. By use of Eq. (18b), it is evident that this aberration is identical to that resulting from the spectral field aberration over a wavelength region given by Eq. (52), as substantiated through ray tracing calculations. This simple equivalence principle holds as long as the off-axis object point moves along the assumed focal surface for which the spectral field aberration has been calculated. Thus, for the case of general hyperbolic grooves or straight grooves, where $L_0' = L_0$, Eq. (14a) describes the wavelength aberration for object points which move along a circle of radius L_0. For the case of tangential focal surfaces, the aberrations are significantly reduced as for spectral field aberrations.

However, in general the focal surfaces of the collecting mirror and the grating will not match, and one must consider a displacement Δx_F of the object point (e.g., the mirror focus) in front of or behind the grating focal surface. Using Eqs. (49) and (50), this is found to yield an aberration

$$\Delta\lambda/\lambda* \simeq 2(\Delta x_F/L_0)/\alpha_0/f_x/(\beta_0^2/\alpha_0^2 - 1). \tag{54}$$

A detector displacement, Δx_D along the direction of the central ray, will give rise to a similar aberration. This can be easily calculated, from the diameter of the ray cone intercepted at the displaced position and the plate scale, to be

$$\Delta\lambda/\lambda* \simeq 2(\beta_0/\alpha_0)^2(\Delta x_D/L_0)/\alpha_0/f_x/(\beta_0^2/\alpha_0^2 - 1). \tag{55}$$

Note that this is a factor of $(\beta_0/\alpha_0)^2$ worse than that due to a comparable displacement of the object point. This factor is obtained by realizing that (a) the diffracted beam is (β_0/α_0) faster than the incident beam, and (b) the effect of a given angular displacement, $\Delta\beta$, is also a factor of (β_0/α_0) larger in wavelength than that due to a displacement $\Delta\alpha$, as derived in Eq. (43).

The effect of grating translational and rotational misalignments can also be studied by appropriate substitution in Eqs. (49)–(51) for the six quantities: $\Delta x, \Delta x', \Delta y, \Delta y', \Delta z, \Delta z'$. For example, a grating pitch τ_y about the y axis leads to the substitution $\Delta z = \Delta z' = -x\tau_y$, resulting in

$$D\lambda/\lambda* \simeq 2\tau_y/\alpha_0/(\beta_0\,\alpha_0 - 1), \tag{56a}$$

$$\Delta\lambda/\lambda* \simeq 4\tau_y(\beta_0/\alpha_0 - 1)/f_x. \tag{56b}$$

The final consideration is the curvature of the detector surface required to minimize aberrations resulting from object points off-axis in the off-plane direction perpendicular to dispersion, i.e., $y \neq 0$. Minimizing the spectral aberrations $\Delta\lambda$, preliminary ray traces reveal a radius of curvature in this direction which is significantly smaller than the optimal radius of curvature within the dispersion plane. Thus, if the grating is to be illuminated off-axis in this direction, a first approximation to the optimal focal surface is a toroid. More detailed results will be reported in a study of echelle grating combinations, where the 2-D wavelength map requires particular attention to the shape of the focal surface.

V. Conclusions

We have presented in detail the imaging properties of several designs for varied line-space gratings in converging beams of light. A common feature to both the in-plane and off-plane solutions is that the imaging does not degrade as the graze angle of reflection vanishes. This is in striking contrast to the behavior of other grazing incidence gratings (e.g., a concave Rowland circle grating) where aberrations rapidly grow at grazing incidence.

For the straight groove designs (whether they are in-plane and parallel or off-plane and in a fan geometry), the dominant aberration is coma. The spectral fields are similar and are improved by use of curved focal surfaces of comparable radii. Astigmatism is linear with wavelength along the sagittal focal surfaces of the straight groove designs.

The main difference between the straight groove designs is the practically attainable resolution, which

depends strongly on the dispersive power. The off-plane design requires significantly higher line densities and is limited in dispersive power by the conical geometry of the diffracted beam. However, the conical mount concentrates the diffracted energy into a single spectral order, and thus may find use as an echelle at high resolution, or in first order at lower resolution than in-plane gratings.

The curved groove designs (in-plane) achieve resolutions comparable with normal incidence gratings. Their geometries are sufficiently symmetric to allow fabrication through either mechanical or holographic rulings. Owing to the plane grating surface, off-axis and grating misalignment aberrations are small, which encourages the design of echelle spectrometers utilizing various combinations of plane gratings with varied line spacings.

Note added in proof. In equation 19, γ_0 is the angle between the incident central ray and the x-axis, as present in the generalized grating equation: $m\lambda*/d_0 = \sin\gamma_0(\cos\beta* - \cos\alpha_0)$; γ_0 is thus also the half-cone angle of the rays diffracted from the central groove."

It is a pleasure to acknowledge John Simmons for developing a computer program which generated some of the tedious series expansions reported in this paper, following the basic algorithm reported by Andersen.[18] I would also like to thank M. Lampton, S. Bowyer, C. Martin, P. Jelinsky, R. Malina, B. Bach, T. Harada, J. Lerner, T. Caruso, E. Loewen, and A. Bunner for helpful discussions and the Berkeley Astronomy Department for the use of their text editing facility. This work was supported by NASA grant NAG 5-420.

References

1. M. C. Hettrick and S. Bowyer, "Variable Line-Space Gratings: New Designs for Use in Grazing Incidence Spectrometers," Appl. Opt. **22,** 3921 (1983).
2. M. V. R. K. Murty, "Use of Convergent and Divergent Illumination with Plane Gratings," J. Opt. Soc. Am. **52,** 768 (1962).
3. M. V. R. K. Murty and N. C. Das, "Narrow-Band Filter Consisting of Two Aplanatic Gratings," J. Opt. Soc. Am. **72,** 1714 (1982).
4. J. T. Hall, "Focal Properties of a Plane Grating in a Convergent Beam," Appl. Opt. **5,** 1051 (1966).
5. J. D. Baumgardner, "Theory and Design of Unusual Concave Gratings," Thesis, U. Rochester (1969).
6. W. C. Cash, Jr., "X-Ray Spectrographs Using Radial Groove Gratings," Appl. Opt. **22,** 3971 (1983).
7. M. Born and E. Wolf, *Principles of Optics* (Pergamon, New York, 1975), pp. 206 and 207.
8. E. G. Loewen and L. Bartle, "Triangular and Sinusoidal Grooves in Holographic Gratings—Manufacture and Test Results," Proc. Soc. Photo-Opt. Instrum. Eng. **240,** 27 (1980).
9. A. J. Caruso, G. H. Mount, and B. E. Woodgate, "Absolute *S*- and *P*-Plane Polarization Efficiencies for High Frequency Holographic Gratings in the VUV," Appl. Opt. **20,** 1764 (1981).
10. G. H. Mount and W. G. Fastie, "Comprehensive Analysis of Gratings for Ultraviolet Space Instrumentation," Appl. Opt. **17,** 3108 (1978).
11. J. Kielkopf, "Echelle and Holographic Gratings Compared for Scattering and Spectral Resolution," Appl. Opt. **20,** 3327 (1981).
12. C. A. Wallace, G. D. Ludbrook, and M. Stedman, "Manufacture and Measurement of Ion-Etched X-Ray Diffraction Gratings," Proc. Soc. Photo-Opt. Instrum. Eng. **315,** 165 (1981).
13. J. Lerner, "Aberration Corrected Holographically Recorded Diffraction Gratings," Proc. Soc. Photo-Opt. Instrum. Eng. **240,** 72 (1980).
14. Y. Sakayanagi, "Ruling of a Curved Grating," Sci. Light **3,** 79 (1955).
15. M. C. Hettrick, "Extreme Ultraviolet Explorer Spectrometer Option Study," MCH/EUVE/321/82, U. California, Berkeley (1982).
16. M. Neviere, D. Maystre, and W. R. Hunter, "Use of Classical and Conical Diffraction Mountings for XUV Gratings," J. Opt. Soc. Am. **68,** 1106 (1978).
17. R. A. M. Keski-Kuha, "Layered-Synthetic Microstructure Technology Considerations for the Extreme Ultraviolet," submitted ??
18. T. B. Andersen, "Automatic Computation of Optical Aberration Coefficients," Appl. Opt. **19,** 3800 (1980).